RESEARCH ARTICLE

Experimental investigation of the inclined interface Richtmyer–Meshkov instability before and after reshock

Jacob McFarland · David Reilly · Skylar Creel ·
Christopher McDonald · Thomas Finn ·
Devesh Ranjan

Abstract An experimental study on the Richtmyer–Meshkov instability (RMI) is presented, which used a new experimental facility at Texas A&M University built for conducting shock-accelerated, inhomogeneous, inclined fluid interface experiments. The RMI develops from the misalignment of the pressure and density gradients for which the inclined shock tube facility is uniquely well suited since a fluid interface can be created at a prescribed angle to the incident shock. Measurements of the evolving RMI are taken using planar laser Mie scattering images for both the pre- and post-reshock regimes, which capture the qualitative evolution of the interface. Statistical measurements demonstrate that the inclined interface initial conditions have a high degree of run-to-run repeatability. The interface mixing width is scaled using the method developed in author's previous work and shows that the non-dimensional mixing width grows linearly in the pre-reshock regime and then levels off at the onset of reshock, after which it grows linearly again. Mie scattering images at late times exhibit the evolution of a secondary shear instability on the primary vortex feature, which has never been resolved in simulations of the inclined interface RMI. A 2D velocity field is obtained for this feature using particle image velocimetry and processed to indicate the strength of the vorticity present. Images of the interface after reshock reveal the inversion of the bubble and spike features and the decay of prominent features toward a turbulent state.

J. McFarland · D. Reilly · S. Creel · C. McDonald · T. Finn ·
D. Ranjan (✉)
Department of Mechanical Engineering, Texas A&M University,
3123 TAMU, College Station, TX 77843-3123, USA
e-mail: dranjan@tamu.edu

1 Introduction

The Richtmyer–Meshkov instability (RMI) (Richtmyer 1960; Meshkov 1972) results from the interaction of an incident shock wave on a density gradient where the two are misaligned. This instability is closely related to the Rayleigh–Taylor instability (RTI) (Taylor 1950) and can be viewed as the limit of RTI where the acceleration becomes impulsive. The interaction of a shock wave with a density gradient produces vorticity through the baroclinic term of the vorticity equation as shown in Eq. 1, where $\vec{\omega}$ is the vorticity, $\mathrm{D}\vec{\omega}/\mathrm{D}t$ is the substantial derivative of $\vec{\omega}$, ρ is the density, P is the pressure, u is the velocity, and v is the kinematic viscosity. From the baroclinic term, it is apparent that the strength of the resulting vorticity is dependent upon the strength of the pressure and density gradients as well as the angle of intersection between them. The strengths of the pressure and density gradients are described by the Mach number and Atwood number, respectively. The Atwood number is a ratio of interface density differences and is shown in Eq. 2, where the subscripts h and l denote high-density and low-density fluids, respectively. In problems where the interface is diffuse, the diffusion thickness is also important in describing the density gradient.

$$\frac{\mathrm{D}\vec{\omega}}{\mathrm{D}t} = \vec{\omega} \cdot \vec{\nabla}\vec{u} + v\nabla^2\vec{\omega} + \left[\frac{1}{\rho^2}\vec{\nabla}\rho \times \vec{\nabla}P\right]_{\text{baroclinic term}}$$

(1)

$$A = \frac{\rho_{\mathrm{h}} - \rho_{\mathrm{l}}}{\rho_{\mathrm{h}} + \rho_{\mathrm{l}}} \text{ (For the light over heavy fluid case)} \quad (2)$$

The RMI has applications in many areas of scientific research such as supersonic combustion (Marble et al. 1990), where the RMI can be beneficial to the mixing of oxidizer and fuel, and stellar phenomena such as the

formation of supernovae (Kane et al. 1999). Research on the RMI has recently been driven largely by its role in inertial confinement fusion (ICF). Inertial confinement fusion (ICF) is being developed as a possible source for electric energy (Kramer et al. 2008) and stellar propulsion (Orth 2003). Energy from ICF could be instrumental in addressing global climate change by providing a large amount of the world's energy demands while producing no carbon emissions. The RMI evolves along with the RTI on the density interfaces of the ICF fuel target (Anderson et al. 2000) reducing the yield by mixing high-density Deuterium–Tritium fuel with low-density fuel or inert ablator material. This mixing reduces the core temperatures and pressures achieved leading to low-energy yields from the target. More in-depth descriptions of the RMI and the research efforts relating to it are provided by Brouillette (2002) and Ranjan et al. (2011).

The RMI has been studied extensively in both experiments and simulations. The methods for creating the necessary ingredients for the RMI (a density and pressure gradient along with a perturbation between them) have varied greatly. To put the current work into the context of the RMI field, a brief description of the past experimental works and their methods is given. To create the pressure gradient, methods such as accelerating the entire experimental apparatus (Chapman and Jacobs 2006) or using a laser-driven shock in a solid (Robey et al. 2001; Harding et al. 2009; Drake et al. 2011) have been used. The most prominent of the laser-driven shock experiment facilities is the National Ignition Facility (NIF) (Robey et al. 2012), which is working to show that ICF can be used as a viable energy source. One of the more common methods, and the method used for the work in this paper, is to use a mechanically generated shock wave in a facility known as a shock tube. In these facilities, a shock front is created by the sudden release of a high-pressure volume, known as the driver, into a low-pressure volume, known as the driven section. With sufficient length, the initial release of the high pressure will result in the coalescence of compression waves into a planar shock front.

The density gradient is created with an interface between two materials of different densities. This gradient can be steep as in the case of two solids or diffuse as in the case of a gas interface with no barriers. The required perturbation between the pressure and density gradients is most commonly created by perturbing the interface, although it can be created by perturbing the shock front (Bailie et al. 2012). One of the earliest methods for creating a perturbed density interface was to use a thin membrane to separate two gases with a prescribed perturbation as used by Meshkov (1972) in his seminal experiments. This method was employed successfully in many other experiments (Vetter and Sturtevant 1995; Houas and Chemouni

1996; Kucherenko et al. 2010) including the shock bubble experiments (Ranjan et al. 2005, 2008, 2011; Niederhaus et al. 2009; Haehn et al. 2011) where the film is composed of a liquid. The membrane method has some drawbacks though, such as the presence of film fragments in the flow, which can distort the fluid field and interfere with optical diagnostic techniques (Erez et al. 2000; Abakumov et al. 1996). To avoid some of the draw backs of using a membrane, membraneless techniques were developed, such as the gas cylinder experiments developed by Jacobs (1992). This technique creates an interface by continuously flowing a heavy (light) gas through a light (heavy) gas in a column from top (bottom) to bottom (top). This perturbation creates a light–heavy–light (heavy–light–heavy) interface. Multiple columns can be coupled together to create interfaces with more complex 2D geometries (Balasubramanian et al. 2012; Prestridge et al. 2000; Mikaelian 1996; Vorobieff et al. 2011). Another method to create a membraneless experiment is to rest a light fluid above a heavy fluid and to co-flow the gases to control diffusion. This configuration remains stable until it interacts with the incident shock wave. Perturbations can be introduced into this interface by shaking the interface (Motl et al. 2009; Collins and Jacobs 2002), by inducing shear on the interface (Weber et al. 2012), or by oscillating the interface from below (Krivets et al. 2009; Long et al. 2009).

The method of interface perturbation chosen for the work presented in this paper is the inclined interface. The inclined interface is set up much like the other stably stratified membraneless experiments discussed previously, but instead of inducing a perturbation to the interface which pulls it out of its stable stratification momentarily, the stable stratification is inclined with respect to the shock wave. This is achieved by tilting a shock tube with respect to gravity so that the interface stays aligned with gravity while the incident shock wave travels at a direction that is inclined to gravity. This perturbation is a simple method that provides a highly repeatable perturbation that directly controls the cross product of the gradient of pressure and density in the vorticity equation, and allows the energy deposition on the interface to be varied without changing the Mach number or Atwood number. Previous work was done using simulations, which examined the effects of inclination angle, Mach number, and Atwood number for before and after reshock (McFarland et al. 2011, 2013). Early experiments were presented briefly in work by Haas (1993) and Sturtevant (1987). A similar interface is encountered in shock refraction work (Jahn 1956; Abd-El-Fattah and Henderson 1978, 2006; Abd-El-Fattah et al. 1976) but the post-shock flow was not the subject of the research. Experiments using an inclined gas cylinder have been presented recently (White et al. 2011), which use similar diagnostics to this work and an inclined shock tube

but have a distinctly different perturbation. Theoretical work and simulations, which focused on the circulation deposited (Samtaney and Zabusky 1994), as well as simulations of an inclined gas curtain, were performed as well (Zhang et al. 2005). Experiments and simulations of the related light–heavy–light chevron-type interface (Smith et al. 2001) and theoretical work on a similar "v-" shaped interface (Mikaelian 2005) have been presented as well.

The case of a twice shocked RMI interface is often created in shock tube facilities through the process of re-shock. A reshock is formed by the reflection of the transmitted shock from the lower boundary of the shock tube to restore the bulk fluid velocity to zero. The reflected shock front then travels back toward the interface and interacts again with the already evolving RMI. This second shock interaction can be used to magnify the instability, enhance mixing, and push the flow field closer to a turbulent state. These types of experiments can be used to study the decay of the RMI into turbulence, where computer models are being pushed to new limits (Hill et al. 2006; Latini et al. 2007).

The purpose of this paper is to report the first experimental results from the Texas A&M University (TAMU) advanced fluid mixing shock tube facility. The capabilities of this new shock tube facility and the experimental procedures will be described. A series of Mie scattering images from times before reshock will be presented along with the measurement of the mixing width and comparison to a scaling model developed with simulations (McFarland et al. 2011). A high temporal resolution series of reshock interface images will also be presented with the analysis and comparison to simulation mixing width growth rates.

2 Experimental facility

The experiments reported in this paper were performed with the TAMU advanced fluids mixing shock tube (Fig. 1). This facility uses a variable inclination design to create an inclined interface perturbation for performing RMI experiments. The internal length of the shock tube is approximately 8.7 m, while the support structure is approximately 9.75 m in length. The tube can be pivoted about its base from horizontal (0°) to fully vertical (90°). It was designed to support incident shock strengths of up to Mach 3.0 into air at atmospheric conditions. The pivoting weight of the shock tube is approximately 20 kN and it is bolted to an isolated concrete slab with a weight of about 45 kN, which aids in resisting the vibrations induced by the shock wave and its reflections. The shock tube was constructed with a support beam and a modular reconfigurable design to allow for the greatest flexibility for future experiments. The major segments can be removed and

reassembled on the beam to allow for upward or downward firing shocks (shocks from light to heavy or heavy to light gasses), or sections can be removed to shorten the tube for different experiments. The tube is moved into place by use of an overhead crane and is supported during operation by a ∼ 6-m-tall steel tube stand bolted to the floor.

The driver section of the shock tube (Fig. 1b) provides the high-pressure volume necessary to initiate and sustain the incident shock wave. This section was constructed of a welded steel tube designed to hold pressures in excess of 2,000 psi. The high pressure in the driver is initially separated from the low-pressure-driven section by a thin piece of sacrificial material known as the diaphragm. The diaphragm is held in place by the hydraulic diaphragm loader (Fig. 1c). This section was originally designed and built by the Sturtevant group at Cal Tech but was donated through the Wisconsin Shock Tube Laboratory to be repurposed in the TAMU shock tube. This section incorporates a hydraulic ram that uses a hydraulic pump to develop over 1,000 kN of clamping force on the diaphragm and allows for the diaphragms to be constructed of strong materials such as mild steels.

A knife edge in the shape of an "x" is contained in the driven side of the hydraulic diaphragm loader and is used to cut the diaphragm as it is pushed against it by high-pressure gas on the driver side. This cutting action helps ensure that the diaphragm fails quickly, releasing the driver gas as fast as possible. Hydraulic return rams were added to the original design to allow used diaphragms to be removed quicker. Once the hydraulic diaphragm loader is disengaged, the driver can be lifted by means of an electric cable wench to allow the diaphragm to be exchanged. The top of the driver section contains instrumentation and two control valves: a slow fill valve and a boost valve. The slow fill valve is used to raise the pressure of the driver slowly without rupturing the diaphragm. In contrast, the boost valve is a fast-acting solenoid valve with a 30-ms opening time that allows an inrush of high-pressure gas to push the diaphragm against the knife edge to its failure point quickly and repeatably.

The driven section (Fig. 1b) is a length of tube, which allows the escaping gas from the driver time to form into a fully planar shock front. Below the driven section is the test section (Fig. 1b). The test section is composed of three subsections: the interface creation section, the test section, and the reshock section. These sections are constructed of bolted 2-in. thick, heat-treated, 4140 steel plates. The bolted construction of these sections allows them to be disassembled and reconfigured for different optical techniques, while still being capable of withstanding shock pressure of over 12 MPa. The test sections were designed with ports, which could contain optically transparent windows or steel flanges. This was done to limit the amount of
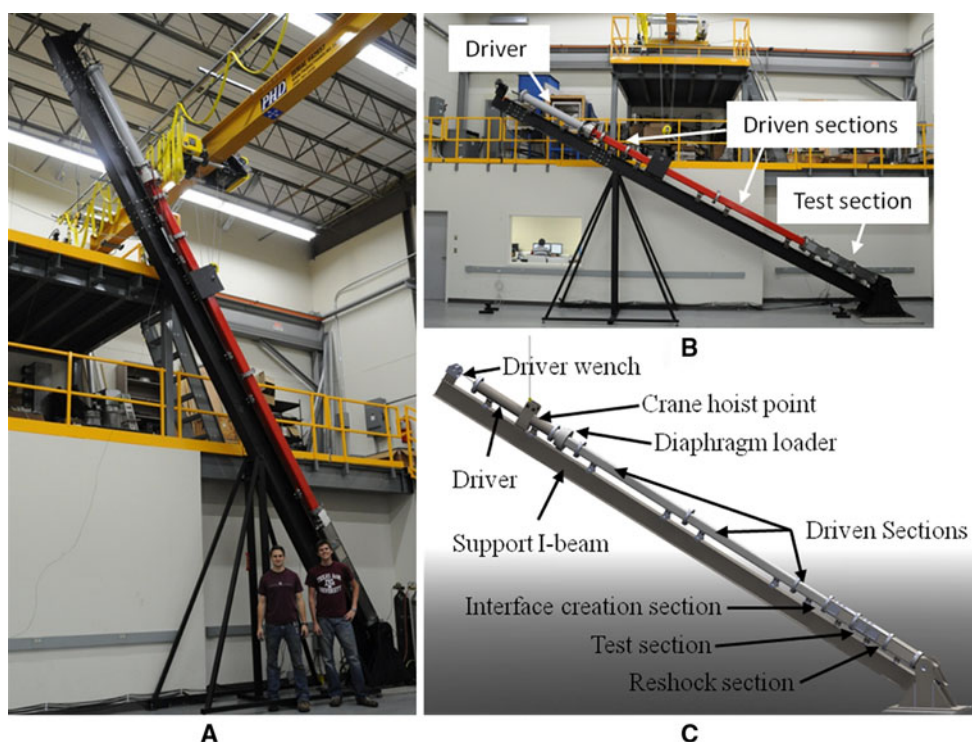
Fig. 1 The Texas A&M University advanced fluids mixing shock tube facility. **a** The shock tube inclined at 60° with authors Chris McDonald (*left*) and David Reilly (*right*) for scale. **b** The shock tube is inclined at approximately 30° with the main sections labeled. **c** An illustration of the shock tube at 30° with all sections labeled
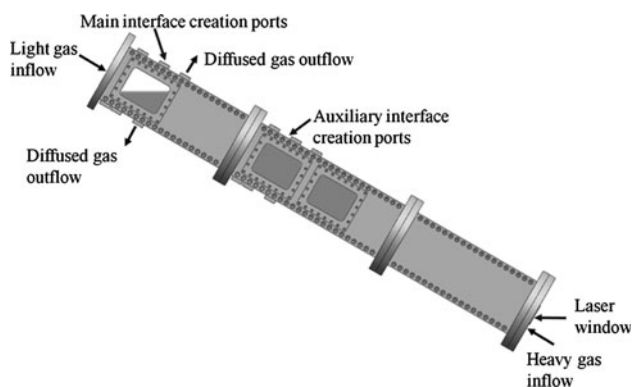

Fig. 2 Illustration of the interface creation method

high-strength glass used in the construction of the shock tube. The window design used in these experiments was a 2-in. thick piece of high optical quality fused silica mounted in a steel flange. These windows are the weakest point in the tube and were designed to withstand up to 12 MPa of dynamic pressure loading from the reshock wave.

The interface creation section contains suction slots that allow the interface diffusion to be limited by co-flowing the light and heavy gasses from the top and bottom of the tube (Fig. 2). The suction slots are used to allow the diffused light and heavy gas mixture at the interface to exit through control valves to the atmosphere. These slots can be reconfigured to different locations for different inclination angles. The initial conditions (IC) section contains two ports for windows to view the interface at the earliest times. The test section was designed primarily for viewing the evolving interface and contains four overlapping window ports. The test section was also designed with the option to use suction ports to create an interface in it as well. The final section in the tube is the reshock section that contains two window ports and was designed for viewing the interface during and after reshock occurs.

The firing of shock waves and the recording of data are managed with a National Instruments (NI) PXIe-6368 multifunction DAQ running with LabVIEW software. This DAQ is capable of both analog and digital input and output and has a maximum sampling rate of 2 million samples per second on up to 16 channels. These channels are used to acquire data from multiple static pressure transducers in the driver and driven sections and from piezoelectric dynamic pressure transducers installed in multiple locations to measure the shock and reshock pressures during an experiment. The dynamic pressure transducers are used for triggering of the camera and laser hardware and used to trigger one of four 32-bit counter timers in the NI hardware. These counter timers are used to precisely trigger the laser pulses and camera CCD operation at a precision of

10 ns. External timing control modules can be used to split these trigger signals again with a precision equal to that of the NI hardware for addition image times. The NI hardware is also used to control six solenoid valves on the tube for filling and firing of the shock wave as well as to control fog and acetone seeding systems.

The camera systems used consist of two TSI Inc. PowerView 1.4 MP cameras that have a short frame straddling time designed for particle image velocimetry (PIV), and two high quantum efficiency TSI Inc. PowerView Plus 2 MP cameras intended for planar laser-induced fluorescence (PLIF) imaging. Both camera sets are equipped with large aperture lenses (f/1.2) that can be fitted with filters for separating PLIF and PIV signals. For the experiments reported in this paper, a dual cavity New Wave Research Gemini PIV laser capable of providing 200 mJ per pulse at 532 nm or ∼ 30 mJ per pulse at 266 nm was used. This laser can be used for PLIF, PIV, and Mie scattering imaging. For future measurements requiring simultaneous PLIF and PIV, a dual cavity Nano PIV Litron laser with a maximum output of 200 mJ/pulse at 532 nm can be used to supplement the PLIF laser system.

The seeding required for PIV or Mie scattering techniques is generated by a Pea Soup fog machine, which creates 0.2–0.3 μm glycerin fog particles using a high-pressure inert gas as a pump. These fog particles have a longer life and lower tendency to condense on surfaces than other fog fluids such as glycol. The ability of these particles to track the flow field was first estimated by finding their relaxation time using the method given by Melling (1997). Equation 3 shows the ratio of the velocity lag between the particles and the fluid at two times where U is the velocity of the fluid (subscript f), or the particle at the initial time after passage of the shock (subscript i), or the time particle at some later time (subscript p). The initial lag velocity ($U_f - U_i$) will be the fluid jump velocity induced by the shock front. By setting this ratio equal to $1/e$, the relaxation time can be calculated as $1/C$. Equation 4 defines the variable C, where v is the kinematic viscosity of the fluid and d is the particle diameter. Performing these calculations, the relaxation time of particles in the CO_2 (the particle in the CO_2 will react slower due to the lower viscosity) will be less than $1E - 9$ s. During this time, the particle will only be able to fall behind the fluid flow by a distance of less than 200 nm, which is below the imaging resolution.

$$\frac{U_f - U_p}{U_f - U_i} = e^{-Ct} \tag{3}$$

$$C = \frac{18v}{d} \tag{4}$$

Another estimate can be made of the ability of the particles to track the velocity fluctuations of the flow using the method of Hjelmfelt and Mockros (1966) and Melling (1997) as it was implemented by Prestridge et al. (2000) for shock tube experiments. Using this method, a criterion was set that the particles energy spectrum had to be within 95 % of the energy spectrum of the gas. A conservative estimate was made by assuming Stokes flow to calculate the drag coefficient of the fog particles. Equation 5 shows the ratio of the energy spectrums for the particles and fluid where E is the energy spectrum of the fluid (subscript f) or particle (subscript p), and S is the ratio of the particle density to the fluid density. Equation 6 defines the Stokes number where ω is the characteristic frequency of the fluid motion. Using these equations, it was found that particles with a diameter of 0.25 μm could track the energy spectrum of the CO_2 (which has the lower viscosity and therefore was more difficult for the particles to follow) within 1 % for a velocity fluctuation frequencies of up to 51 kHz.

$$\frac{E_p}{E_f} = \frac{(18Sk^2/S)^2}{(18Sk^2/S)^2 + 1} \tag{5}$$

$$Sk = \sqrt{\frac{v}{\omega d}} \tag{6}$$

Following the methods of Prestridge et al. (2000), the maximum velocity fluctuation frequency that could be tracked by the imaging system was estimated as the fluctuating velocity divided by the PIV grid size. The fluctuating velocity was found using the standard deviation of the fluid velocities found by finding the average of the velocities across the y direction (parallel to the shock front) at each x location (perpendicular to the shock front) of the PIV data. The maximum standard deviation from a late time PIV data set, where the velocity fluctuations were largest, was used. The PIV grid size (0.46 mm) was determined by the PIV bin size and the pixel resolution (discussed further in Sect. 4.4). The maximum velocity fluctuation frequency that could be tracked by the imaging system was estimated to be 48 kHz. With this estimate, it can be seen that the ability of the particles to track the flow is sufficient to track 95 % of the energy spectrum of the fluid. If the criteria to follow the fluid energy spectrum were raised to 99 %, we estimate that particles sizes would need to be 0.2 μm, which is at the edge of particle size distribution given by our seeding system.

3 Experimental method

The RMI experiments in this paper were run with a N_2 over CO_2 interface, an incident shock strength of Mach 1.55, and an inclination angle of 60° (Fig. 3). The inclination angle of the tube was set by using the overhead crane to raise the tube to the correct angle. The tube stand was then
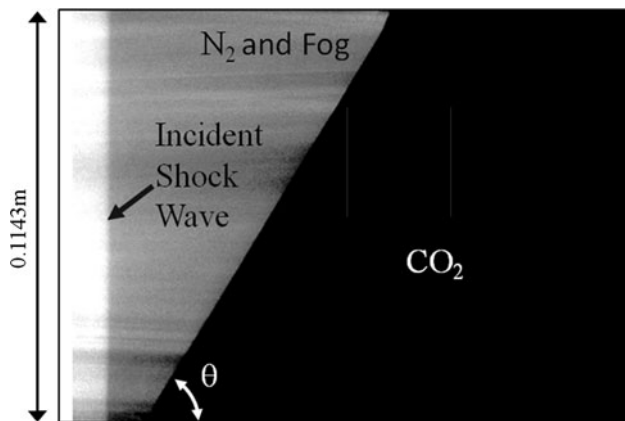
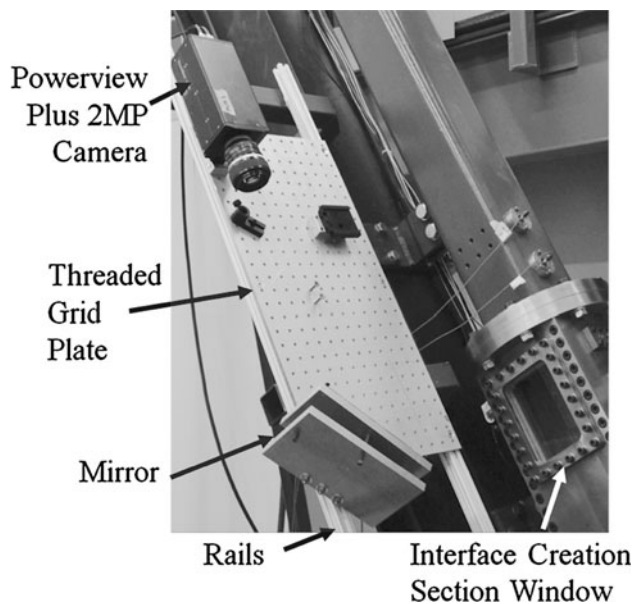Fig. 3 Mie scattering image taken prior to shock wave interface interaction

Fig. 4 Threaded grid and rail mounting system for cameras

installed to hold the shock tube at the prescribed angle, and after releasing the shock tube from the crane, the angle was again measured. A digital inclinometer with an accuracy of ±0.05° was used to measure the angle and was calibrated before each use.

Before the tube is filled, the cameras and lasers are calibrated for imaging in the windows to be imaged. A calibration block is inserted into the tube at each image location, which is used to focus the cameras and check their alignment. The need for the calibration of the cameras is minimized by using a threaded grid and rail mounting system, which can traverse a rail system to be located at different windows (Fig. 4). The location on the rails is set for each window using a metal arm that is temporarily installed and connects the window flange to threaded grid.

This arm prevents the threaded grid from traversing more than ±0.050 in. out of alignment with the window. An optical quality metallic aluminum mirror is used to allow the cameras to be mounted at a 90° angle. The laser is run through a spherical convex lens and a plano-concave lens to create a sheet of laser light. The focal lengths of these lenses are changed for each window location to get the maximum laser power and the minimum sheet thickness. The laser alignment is then checked inside the tube using a calibration target. After calibration is performed for the cameras and lasers, a series of images of the interface are taken as the tube is filled with seeded gas to check the image quality.

The Mie scattering technique is used to visualize the fluid interface in the tube and for acquiring PIV image sets as well. The light gas (nitrogen) is seeded with fog particles using the fog equipment described in the previous section. This fog is mixed with the nitrogen in an external sealed container with a volume, which is large (~ 8 ft^3) relative to the volume of nitrogen contained in the shock tube. This box contains a stirring device to aid in mixing the fog and the nitrogen before it enters the tube. The fog density is controlled by cycling the fog machine using the NI hardware and LabVIEW program. The N_2 and CO_2 flow rates (~ 6 and ~ 3 L/min, respectively) are measured and set to achieve an interface with minimum diffusion while not having any visible shear. The tube is then allowed to fill for 20–30 min to achieve a uniform fog seeding in the nitrogen.

The incident Mach number target is Mach 1.5 but is limited by the diaphragm material and thickness availability. The diaphragm material chosen for these experiments is a polycarbonate sheet with a thickness of 0.030 in. This diaphragm has a dynamic rupture pressure of approximately 102 psi and drives a Mach 1.55 incident shock wave into atmospheric pressure nitrogen. For each experiment, the driver section is pressurized to 70 psi initially to keep the diaphragm just short of a static failure. To fire the shock wave, a precise sequence of valve activation is executed using the LabVIEW program. The fill valves are first shut to allow the interface to settle and the initial shock tube pressure (approximately 0.3 psig) to decrease. After 100 ms, the boost valve is activated and interface suction valves are closed. The boost valve opens fully under 30 ms and the pressure rises to 102 psi, rupturing the diaphragm, within 400 ms of the valve activation. At 500 ms after boost valve activation, the valve is shut off and is fully closed within 50 ms.

The incident shock is formed in the driven section and its speed is then measured using two of the dynamic pressure transducers placed in the driven section just upstream of the interface creation section. The speed was found based on the time at which each transducer read the shock pressure rise

and the distance between the two transducers. Pressure measurements from the dynamic pressure transducers are checked and compared for each experiment, and show a steep pressure gradient with a rise time of less than 5 μs. Images of the incident shock wave using the Mie scattering technique also show a well-formed planar shock wave (Fig. 3). The pressure rise recorded by the dynamic pressure transducers is also used to trigger counter timers in the LabVIEW hardware, which are used to trigger the lasers and cameras at times when the interface will be visible to the cameras through their respective windows.

After each experiment, the tube is vented to atmosphere and the diaphragm exchanged for a new one. The windows are inspected for fog condensation buildup and are cleaned if needed. The lower laser window of the tube is also cleaned of any fog condensate, and on rare occasions when diaphragm debris is found, it is removed. Data and images are processed before running the next shock wave to ensure that the shock tube is functioning properly.

4 Experimental results

4.1 Repeatability and quantification of initial conditions

One of the advantages of the inclined interface shock tube facility, as discussed before, is that it produces highly repeatable IC but, as with any experiment, it is subject to some variation in conditions from run to run. While IC variations have been discussed little in the past literature, they are important for ensemble averaged data sets that we will use. We will attempt to quantify some of the variations in IC to show the strengths of the inclined interface shock tube facility for obtaining statistically converged data sets. We will also describe the IC in detail and the ways in which they depart from the ideal inclined interface RMI. To highlight the variations in IC, eight Mie scattering images were obtained at a time of 10 μs after shock interaction with the interface. These images were used to produce a coefficient of variation plot, Fig. 5. The coefficient of variation highlights areas where the standard deviation is high relative to the average. It can be seen in Fig. 5 that the highest coefficient of variation is due to the interface position that varies up to 1.4 mm in these runs. The shock position variation can also be seen as an area of slightly elevated coefficient of variation that is in agreement with our dynamic pressure transducer data, which shows a typical variation in shock speed of ±2 m/s from ∼540 to ∼544 m/s with a standard deviation of 2.3 m/s over 100 + runs.

One reason for the variation in interface position, shown by Fig. 5, is that the interface departs from the perfect 60°
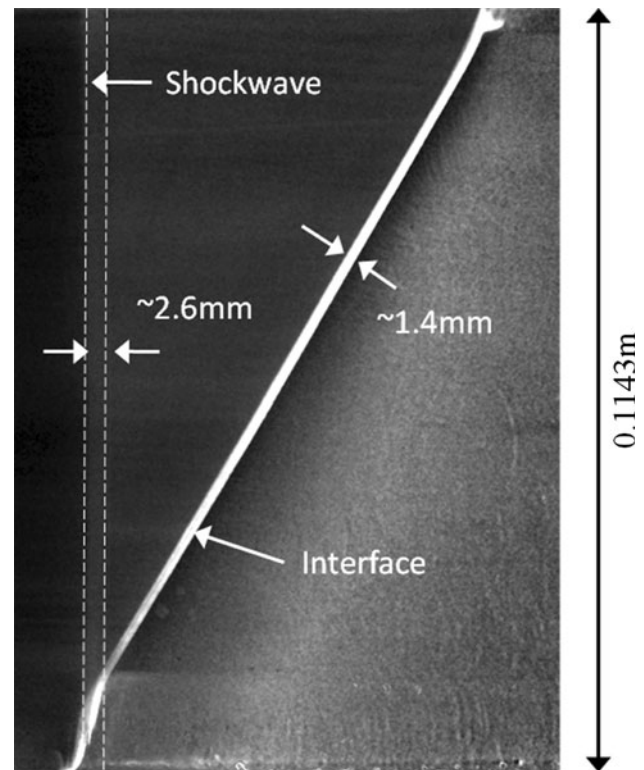

Fig. 5 Coefficient of variation of Mie scattering image intensity from eight experimental runs at $t = 0.01$ ms after shock interaction. The region of variation due to the shock wave position is *highlighted* using a *dashed line* due to its low contrast

inclination during the time it takes for the driver diaphragm to rupture and the shock to reach the interface. This time can be limited to reduce the interface drift during this time, but some departure from the 60° angle is always present. To highlight this drift, a run with a high drift period was imaged just before the shock wave reached the interface. This image was processed to highlight its departure from the 60° inclination plane and is shown in Fig. 6. In Fig. 6c, areas of black (white) show where the interface rose above (below) the inclination plane. In this worst-case scenario, it can be seen that the interface can rise or fall ∼1 mm, while typical values are much lower. A small spike at the lower suction slot is also apparent and is created by an air hammer effect of the valve closing. A small amount of curvature is also created at the interface edges as the velocity vectors of the exiting gas align to the suction slots that are perpendicular to the tube walls. This effect can be minimized by decreasing the gas flow rates, but low flow rates also allow for longer residence times at the interface and a larger diffusion thickness. Figure 7 shows PIV vectors obtained at the interface before an experiment. These vectors show velocities of up to 1.7 cm/s at the interface and a low-velocity back circulation at the edges of the interface. The effect of the interface velocities on the RMI is negligible since they are five orders of magnitude smaller

Fig. 6 **a** The interface position with the suction valves open, **b** the interface position with the suction valves closed after being allowed the maximum drift time before shock interaction, **c** a close-up of the interface highlighting its departure from a 60° plane
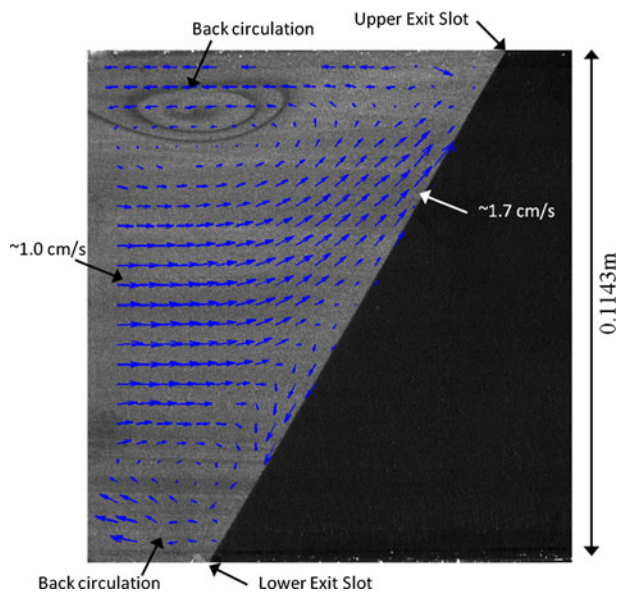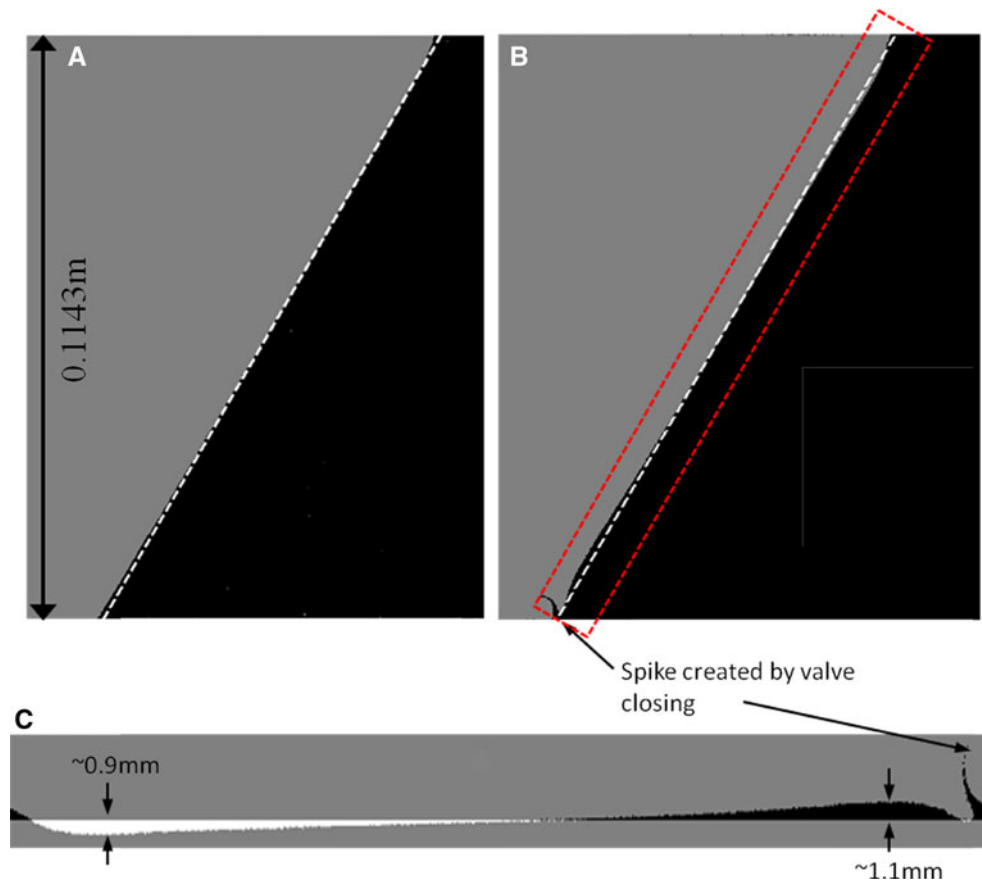

Fig. 7 Velocity vectors at the interface before shock interaction obtained using PIV

than the post-shock interface velocity ($\sim$250 m/s). The departures from the perfect inclination plane can be minimized by controlling flow rates, minimizing drift time, and by improvements in the suction slot design, which will be implemented in future runs.

The interface diffusion thickness was quantified using Mie scattering images taken just before the shock interaction. A line of pixel intensities normal to the interface and extending approximately 25 mm to either side was taken to measure the diffusion thickness. To smooth the random fluctuations in the data, the data were averaged with 30 lines to each side. The pixel intensities increased linearly across the image coupled with an error function discontinuity at the interface. The linear trend in the image intensities is created by the accumulation of light scattered by adjacent fog particles. When the linear trend was removed from the data, the error function could then be fitted and used to determine the 1–99 % concentrations of fogged nitrogen. This showed a diffusion thickness of approximately 1.2 mm (Fig. 8). As mentioned above, this diffusion thickness can be decreased by increasing the gas flow rates, but this risks inducing a shear instability at the interface due to the increased velocities at the interface.

4.2 Qualitative examination of the interface evolution

Having examined the IC for the inclined interface RMI and the repeatability of these conditions, the interface evolution will now be examined in a qualitative manner. Figure 9 shows a time series of images obtained using the Mie
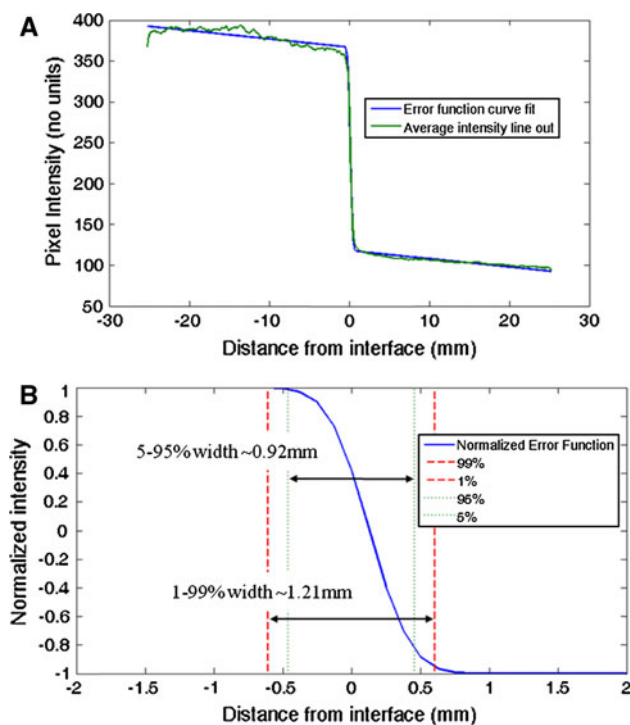
Fig. 8 **a** Pixel intensities plotted from an average of 61 lines of data across the interface showing a linearly increasing error function fitted to the data. **b** The error function fitted to the data showing the 1–99 % concentration of fogged nitrogen

scattering technique. These images were processed to normalize intensities and to remove background noise. The times measured are from the moment the shock wave first intersects the interface. At time 0.01 ms, the shock wave is apparent as a jump in the fog Mie scattering intensity. At the next time ($t = 0.36$ ms), the interface is still entirely in the visible portion of the first window. A bright spot of fog at the lower wall suction slot is also visible. This bright spot is created by the shock interaction with the suction slot that re-suspends condensed fog fluid (glycerin) that had collected in the slot. This spot does not enter the field of view again until reshock occurs, but is a deleterious effect that will be mitigated later by improved suction slot design. Also, at this time, two inflections in the interface curvature can be seen developing. Later, at time 1.19 ms, these inflections have increased in number and amplitude as the vorticity imparted by the RMI is beginning to shape the interface. A small spike preceding what will become the main vortex is also evident at this time but dies out later as it merges with the boundary layer.

At time 2.44 ms, the primary vortex is now prominent and two small vortices (the secondary and tertiary vortices) can also be seen developing from the inflections seen at earlier times. At times 2.91 and 3.38 ms, the secondary and tertiary vortices can be seen developing and merging. By time 3.85 ms, these vortices are on top of each other, and

by time 5.09 ms, they have fully merged. At time 3.38 ms, the upper boundary layer has become fully visible. This feature is always present in the flow but its visibility varies in the images due to the fog concentrations and image normalization procedures used. At time 3.85 ms, another inflection is visible at the tip of the spike. This feature may be a "forking" of the spike as seen in other simulations (Bailie et al. 2012) coupled with a growing boundary layer but this feature has little time to evolve before reshock occurs at approximately 5.64 ms. At time 5.09 ms, many smaller, self-similar Kelvin–Helmholtz vortices can be seen developing on the primary vortex. These features are induced by the strong shear, which exists in this feature between the CO_2 and N_2. Figure 12 in a later section shows a close-up of the features. These features have never been resolved in the simulations of the inclined interface.

The first image in Fig. 10 ($t = 5.64$ ms) shows the interface after the incident shock wave has reflected from the bottom of the tube and reintersected the interface, this time moving from the heavy gas to the light gas. The vorticity is amplified by reshock, and small-scale vortices can be seen developing from perturbations in the pre-re-shock interface. At $t = 6.04$ ms, the primary, secondary, and tertiary vortices have merged with the bubble and become less defined as they dissipate their energy. At 6.44 ms, the process of reshock can be seen to have inverted the interface where now the former spike region containing the vortices has been pushed to an area just out of the frame of view while the bubble region has been inverted and now resembles a spike structure. On this spike, multiple small secondary instabilities can be seen as they grow to larger scales. The boundary layer is also drawn out to mix with the fogged nitrogen by vortex features created by reshock. At this time, the deleterious effects of the incident shock interacting with the lower suction slot can be seen in the region of bright fog at the bottom of the frame. This region is the reshocked bright spot last seen at time 0.36 ms emanating from the lower suction slot. At times $t = 6.84$ ms through 7.64 ms, the spike continues to grow as the bright area of fog from the suction slot becomes more apparent. Again, future improvements to the slot design will mitigate this effect. The small structures created by the process of reshock are now working at late times to break the interface down into smaller and smaller structures, increasing its mixing rate and moving it toward a turbulent state. The reshock spike structure also begins to fork at these late times producing a flat leading edge. The spike also begins to separate into a mixing region and a more homogeneous region of CO_2 at the spike base similar to the results seen in the previous computational work (McFarland et al. 2011). The effects of reshock and the decay of the interface to turbulence will be the subject of a future work.
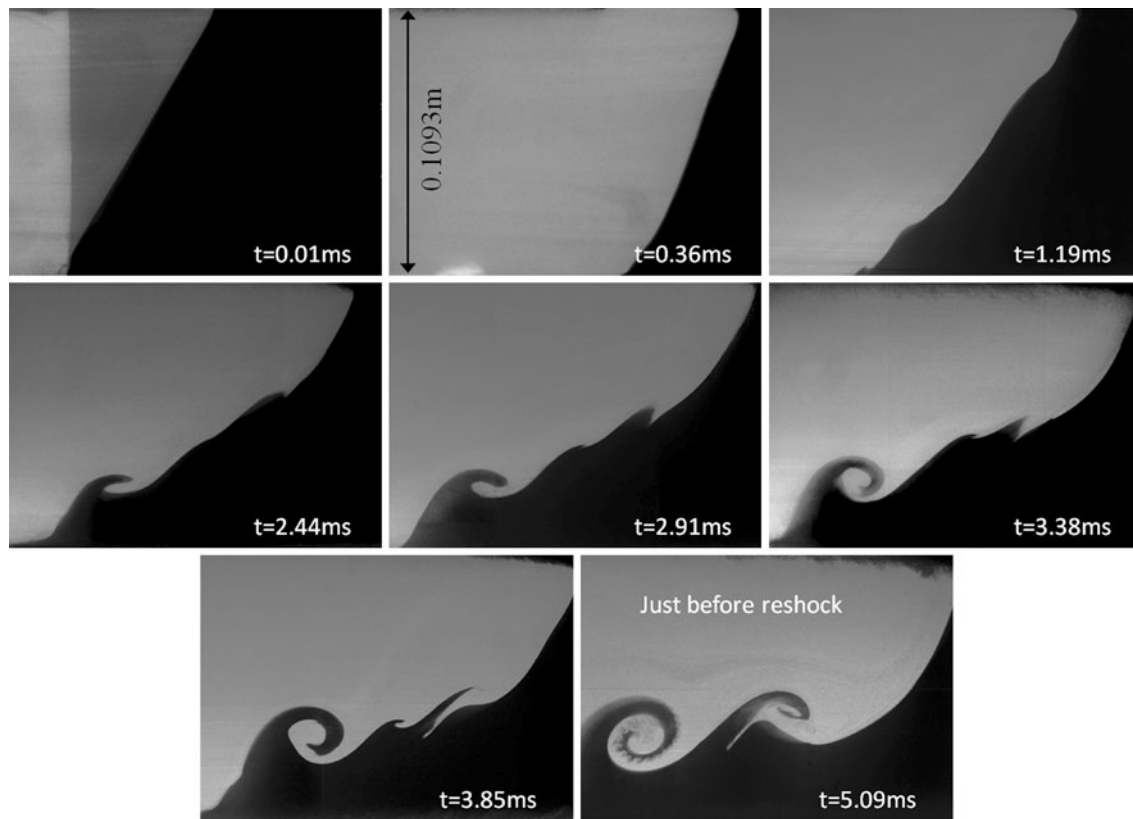
Fig. 9 Time series of Mie scattering images of the inclined interface RMI before reshock
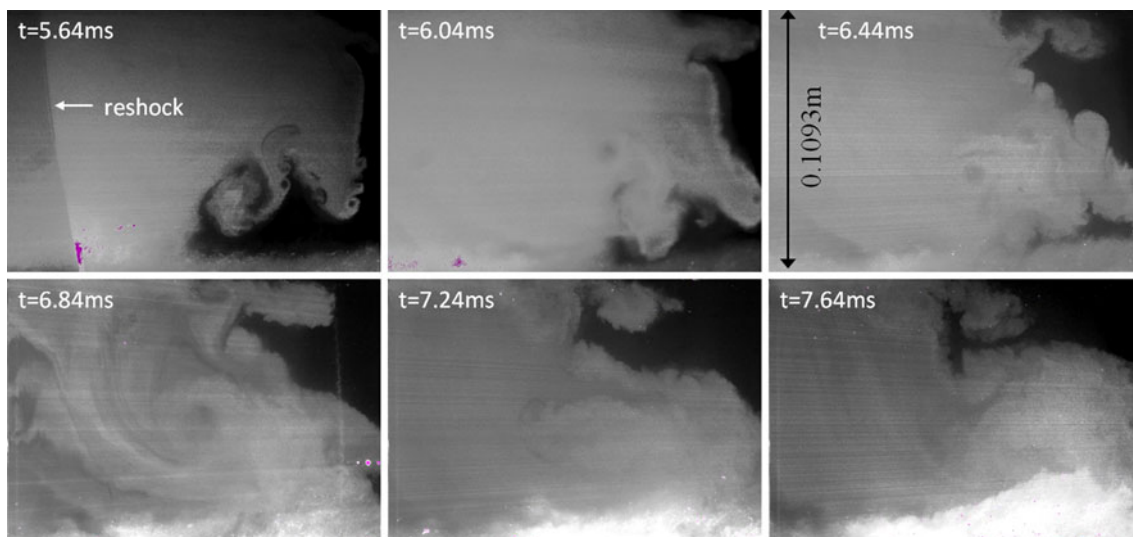

Fig. 10 Time series of Mie scattering images of the inclined interface RMI after reshock

4.3 Mixing width measurements

Having qualitatively examined the evolution of the inclined interface RMI, we now move to making quantitative measurements of the interface growth rate. To do this, we measure the mixing width as defined by the 5–95 % contours of the fogged nitrogen. This is the method used in the previous work by the author (McFarland et al. 2011), and we will follow the scaling method reported in this work as well for the pre-reshock regime. The 5 and 95 % contours were found using the Mie scattering images shown in Fig. 9. These images were processed further to identify the

interface gradient and divide the image into a binary field showing each pixel as N_2 or CO_2. The average intensity along the y direction was taken for each x location to determine when the flow field contained 5 and 95 % CO_2. For the reshock images presented in Fig. 10, the mixing widths could not be estimated using the 5–95 % contours because the contrast at the interface between the CO_2 and the N_2 was greatly reduced by the additional small-scale structures and mixing produced by reshock. This made it difficult to identify the 5 and 95 % contours. The mixing width was instead estimated by finding the leading and trailing edges of the most organized structures upstream and downstream.

To enable comparisons to the previous simulations performed by the author and to future experiments at different Atwood numbers, Mach numbers, and inclination angles, the mixing width and time were non-dimensionalized using the scaling method developed in the author's previous work. Equations 7–11 outline the non-dimensionalizing method. In brief, the non-dimensional time (τ) is zero at the moment its first transverse wall reflection has completely passed through the interface. This time is predicted by t_a^* in Eq. 11 where w_i is the incident shock speed, λ is the interface wavelength, and w_{rrt} is the velocity of the interface reflected, wall reflected, interface transmitted shock speed. The offset time is then non-dimensionalized (in Eq. 10) using the transmitted wave speed w_t, the post-shock Atwood number (A'), and the effective interface wavelength (λ_E in Eq. 8). The interface mixing width is non-dimensionalized using the mixing width at the offset time (Eq. 9), and the effective interface wavelength (Eq. 7).

$$\bar{\eta} = \frac{(\eta - \eta^*)}{\lambda_E} \tag{7}$$

$$\lambda_E = \lambda \cdot \tan(\theta) \tag{8}$$

$$\eta^* = \eta\left(t_a^*\right) \tag{9}$$

$$\tau = \frac{w_t A'}{\lambda_E}\left(t - t_a^*\right) \tag{10}$$

$$t_a^* = \frac{\lambda}{2 w_i \tan\theta} + \frac{\lambda}{2 w_{rrt}} \tag{11}$$

The non-dimensional mixing width measurements are plotted in Fig. 11 with a line of best fit for both the pre- and post-reshock regimes. For the pre-reshock regime, error bars are plotted using the error estimated from image processing and from run-to-run variations. The image processing error is an estimation of the error in identifying the interface based on the variations in image processing that occur and is near 1 % for all data points. The run-to-run variation error was estimated using data from three runs at various times and was estimated to increase linearly
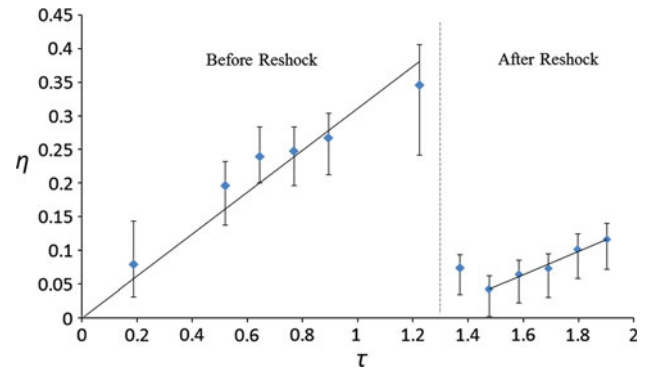

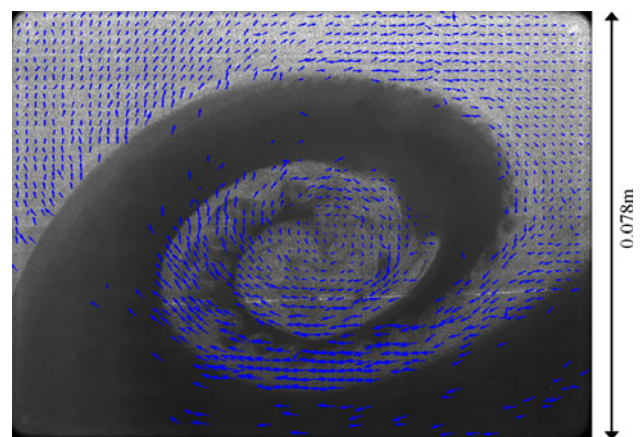**Fig. 11** Non-dimensionalized mixing width plotted versus non-dimensional time

Fig. 12 PIV image with a sample of velocity vectors

from ~ 3.5 % at $t = 1.19$ ms to ~ 5 % at $t = 5.45$ ms. For the mixing width measurement taken at 5.45 ms, the interface mixing width exceeded the visible field of the window and so measurements were estimated using images from just before and after 5.45 ms where the downstream and upstream limits of the mixing width were visible. These measurements were combined using the position of the primary vortex as a reference. The error of this process was also estimated and contributed to the much larger error in this measurement.

For the post-reshock regime, a similar run-to-run error was included as well as an error associated with estimating the mixing width using the necessary modified method described at the beginning of this section for the post-reshock flow field. This method was found to result in a 1 % bias toward a larger than actual mixing width measurement found using pre-reshock calibration images. Based on the mixing width measurements from simulations in the author's previous work (McFarland et al. 2011), a linear trend is expected at early times with a leveling off near the approach of reshock. The measurements shown here

exhibit a linear trend at early times and an asymptotic trend at late times as expected for the pre-reshock regime. In the post-reshock regime, the non-dimensionalized mixing width levels off as expected and then increases linearly. In the future work, these measurements will be compared with simulations and experiments at differing conditions.

4.4 Velocity measurements in the primary vortex

At late times, the primary vortex exhibits a high degree of vorticity with small KH structures developing along the edge of the primary vortex. The primary vortex contains the largest amount of vorticity in the flow field. This vorticity was estimated using velocity vectors obtained using PIV. In an effort to capture some of the vorticity contained in the smaller KH structures, the camera field of view was reduced to contain only the primary vortex. Fog droplets were used as the PIV particles, and a time delay of 2 μs between PIV images was applied to obtain velocity vectors in the flow field that was traveling at a bulk velocity predicted by 1D gas dynamics to be 250 m/s. The vectors were calculated using the TSI software Insight 3G with a
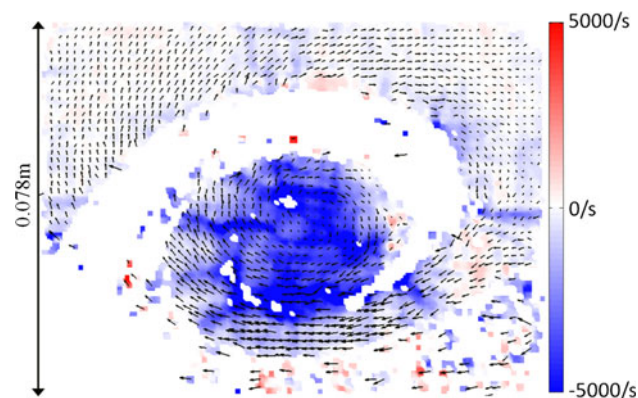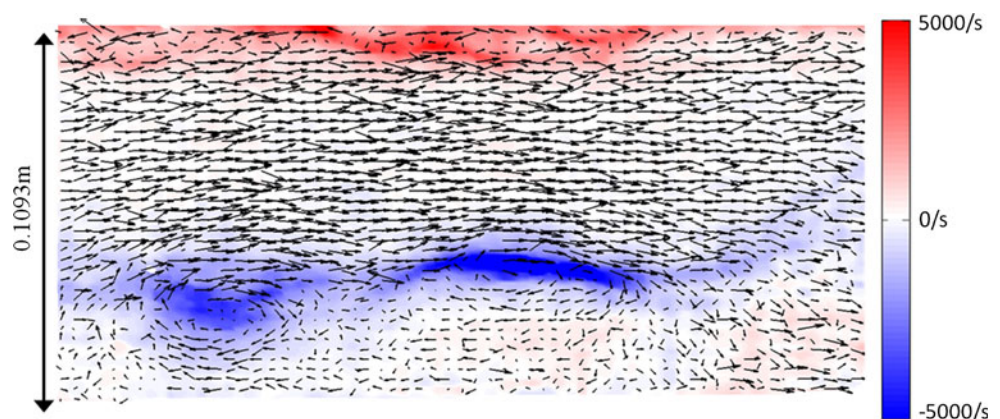
recursive Nyquist grid with a minimum spot size of 8-by-8 pixels, fast Fourier transform (FFT) correlation and Gaussian mask. The vectors obtained had a signal-to-noise pass ratio of 2.0. The bulk velocity was subtracted from the vectors to show the relative motion of the flow field. Figure 12 shows these vectors plotted on top of a processed PIV image where only 1 out of every 9 of the approximately 12,000 vectors obtained are plotted.

The vorticity was plotted by taking the curl of the 2D velocity field. Obtaining numerical derivatives was complicated due to the somewhat noisy vector field. Missing values were first interpolated where nearby points were available. To obtain more accurate numerical derivatives, the vector field was then smoothed using a median filter with a 19-by-19 bin size. The derivatives were then found using the central difference method and combined to find the vorticity field. The vorticity field was again smoothed using a 3-by-3 median filter for the purpose of plotting only. The result is shown in Fig. 13 with a sample of the PIV vectors plotted as well. Figure 13 shows a well-defined vortex core with some regionally high pockets of negative vorticity along the interface possibly due to the KH structures being picked up. Localized spots of positive vorticity were picked up by the occasional vectors found in the unseeded CO_2, but these are likely numerical artifacts of the relatively few points available for numerical differentiation.

The vorticity was also plotted for the entire flow field with velocity vectors superimposed after the subtraction of the bulk velocity as seen in Fig. 14. Velocity vectors were obtained for the bottom region by introducing a small amount of seeded N_2 into the CO_2. The amount of N_2 added to the CO_2 was found to be negligible because the interface was in the location predicted by 1D gas dynamics and prominent feature locations were within run-to-run variation. The interface is associated with a region of negative vorticity with notably less vorticity at the tip of the bubble. Positive vorticity dominates the upper

Fig. 13 Velocity vectors plotted with estimated vorticity field for the primary vortex

Fig. 14 Velocity vectors plotted with estimated vorticity field for the entire flow field

boundary layer and is also seen in other localized regions of the flow field. A region of negative vorticity is expected in the bottom boundary layer, but it is not visible due to light seeding.

5 Conclusions

A new inclined shock tube facility for studying the Richtmyer–Meshkov instability has been completed and preliminary results reported. The Texas A&M shock tube facility has the capability to perform up to Mach 3.0 shock experiments at inclination angles of 0°–90°. This facility was designed for obtaining statistical data sets and is capable of running up to 30 experiments a day using optical diagnostics to obtain the velocity and density field measurements. The first known detailed experiments on the inclined interface Richtmyer–Meshkov instability have been reported. The experiments were shown to have good repeatability with low variation in the IC from run to run. Mie scattering images were used to quantify the initial interface shape, and PIV vectors were obtained to show the negligible interface velocities created by the gas co-flowing method used to create the interface. The initial diffusion thickness was found to be approximately 1.4 mm.

A time series of images obtained over the evolution of the interface shows a strong primary vortex with a secondary and a tertiary vortex, which merge at late times. Images obtained just before reshock show high-resolution KH vortices that develop on top of the primary vortex. These features have never been resolved in previous simulations of the inclined interface RMI. Images of the post-reshock interface show an inversion of the interface and an amplification of small vortical structures, which increase the interface mixing greatly. At late times after reshock, a well-formed spike structure is apparent coupled with strong secondary instabilities, which continue to mix the flow field and drive it further toward a turbulent state. Non-dimensionalized mixing width measurements show an initially linear non-dimensional growth rate of the mixing width followed by an asymptotic period before reshock occurs. Finally, PIV vectors were obtained in the primary vortex and for the whole interface at late time and used to calculate the vorticity. These vorticity plots showed a well-organized core of negative vorticity in the primary vortex with little to no positive vorticity in the interface mixing region.

References

Abakumov AI, Fadeev VY, Kholkin SI, Meshkov EE, Nikiforov VV, Nizovtzev PN, Sadilov NN, Sobolev SK, Tilkunov VA, Tochilin VO et al (1996) Studies of film effects on the turbulent mixing zone evolution in shock tube experiments. In: Young R, Glimm J, Boston B (eds) Proceedings of the fifth international workshop on compressible turbulent mixing. World Scientific, Singapore, p 118

Abd-El-Fattah AM, Henderson LF (1978) Shock waves at a slow–fast gas interface. J Fluid Mech 89:79–95

Abd-El-Fattah AM, Henderson LF (2006) Shock waves at a fast–slow gas interface. J Fluid Mech 86:15–32

Abd-El-Fattah AM, Henderson LF, Lozzi A (1976) Precursor shock waves at a slow–fast gas interface. J Fluid Mech 76:157–176

Anderson MH, Puranik BP, Oakley JG, Brooks PW, Bonazza R (2000) Shock tube investigation of hydrodynamic issues related to inertial confinement fusion. Shock Waves 10:377–387

Bailie C, McFarland JA, Greenough JA, Ranjan D (2012) Effect of incident shock wave strength on the decay of Richtmyer–Meshkov instability-introduced perturbations in the refracted shock wave. Shock Waves 22:511–519

Balasubramanian S, Orlicz GC, Prestridge KP, Balakumar BJ (2012) Experimental study of initial condition dependence on Richtmyer–Meshkov instability in the presence of reshock. Phys Fluids 24:034103

Brouillette M (2002) The Richtmyer–Meshkov instability. Annu Rev Fluid Mech 34:445–468

Chapman PR, Jacobs JW (2006) Experiments on the three-dimensional incompressible Richtmyer–Meshkov instability. Phys Fluids 18:074101

Collins BD, Jacobs JW (2002) PLIF flow visualization and measurements of the Richtmyer–Meshkov instability of an air/SF6 interface. J Fluid Mech 464:113–136

Drake RP, Doss FW, McClarren RG, Adams ML, Amato N, Bingham D, Chou CC, DiStefano C, Fidkowski K, Fryxell B, Gombosi TI, Grosskopf MJ, Holloway JP, van der Holst B, Hunting CM (2011) Radiative effects in radiative shocks in shocktubes. High Energy Density Phys 7:130–140

Erez L, Sadot O, Oron D, Erez G, Levin LA, Shvarts D, Ben-Dor G (2000) Study of the membrane effect on turbulent mixing measurements in shock tubes. Shock Waves 10:241–251

Haas JF (1993) Experiments and simulations on shock waves in non-homogeneous gases. In: Proceedings of the 19th international symposium on shock waves. Springer, Marseille, pp 27–36

Haehn N, Weber C, Oakley J, Anderson M, Ranjan D, Bonazza R (2011) Experimental investigation of a twice-shocked spherical gas inhomogeneity with particle image velocimetry. Shock Waves 21:225–231

Harding E, Hansen J, Hurricane O, Drake R, Robey H, Kuranz C, Remington B, Bono M, Grosskopf M, Gillespie R (2009) Observation of a Kelvin–Helmholtz instability in a high-energy-density plasma on the omega laser. Phys Rev Lett 103:045005

Hill DJ, Pantano C, Pullin DI (2006) Large-eddy simulation and multiscale modelling of a Richtmyer–Meshkov instability with reshock. J Fluid Mech 557:29

Hjelmfelt AT Jr, Mockros LF (1966) Motion of discrete particles in a turbulent fluid. Appl Sci Res 16:149–161

Houas L, Chemouni I (1996) Experimental investigation of Richtmyer–Meshkov instability in shock tube. Phys Fluids 8:614

Jacobs JW (1992) Shock-induced mixing of a light-gas cylinder. J Fluid Mech 234:629–649

Jahn RG (1956) The refraction of shock waves at a gaseous interface. J Fluid Mech 1:457–489

Kane J, Drake RP, Remington BA (1999) An evaluation of the Richtmyer–Meshkov instability in supernova remnant formation. Astrophys J 511:335–340

Kramer KJ, Latkowski JF, Abbott RP, Boyd JK, Powers JJ, Seifried JE (2008) Neutron transport and nuclear burnup analysis for the laser inertial confinement fusion–fission energy (LIFE) engine. Fusion Sci Technol 56:625–631

Krivets VV, Long CC, Jacobs JW, Greenough JA (2009) Shock tube experiments and numerical simulation of the single mode three-dimensional Richtmyer–Meshkov instability. In: 26th international symposium on shock waves. Springer, Gottingen, pp 1205–1210

Kucherenko YA, Pavlenko AV, Shestachenko OE, Balabin SI, Pylaev AP, Tyaktev AA (2010) Measurement of spectral characteristics of the turbulent mixing zone. J Appl Mech Tech Phys 51:299–307

Latini M, Schilling O, Don WS (2007) Effects of WENO flux reconstruction order and spatial resolution on reshocked two-dimensional Richtmyer–Meshkov instability. J Comput Phys 221:805–836

Long CC, Krivets VV, Greenough JA, Jacobs JW (2009) Shock tube experiments and numerical simulation of the single mode three-dimensional Richtmyer–Meshkov instability. Phys Fluids 21:114104

Marble FE, Zukoski EE, Jacobs JW, Hendricks GJ, Waitz IA (1990) Shock enhancement and control of hypersonic mixing and combustion. American Institute of Aeronautics and Astronautics, Orlando, FL

McFarland J, Greenough J, Ranjan D (2011) Computational parametric study of a Richtmyer–Meshkov instability for an inclined interface. Phys Rev E 84:026303

McFarland JA, Greenough JA, Ranjan D (2013) Investigation of the initial perturbation amplitude for the inclined interface Richtmyer–Meshkov instability. Phys Scr T155:014014

Melling A (1997) Tracer particles and seeding for particle image velocimetry. Meas Sci Technol 8:1406

Meshkov EE (1972) Instability of the interface of two gases accelerated by a shock wave. Fluid Dyn 4:101–104

Mikaelian KO (1996) Numerical simulations of Richtmyer–Meshkov instabilities in finite-thickness fluid layers. Phys Fluids 8:1269–1292

Mikaelian KO (2005) Richtmyer–Meshkov instability of arbitrary shapes. Phys Fluids 17:034101

Motl B, Oakley J, Ranjan D, Weber C, Anderson M, Bonazza R (2009) Experimental validation of a Richtmyer–Meshkov scaling law over large density ratio and shock strength ranges. Phys Fluids 21:126102

Niederhaus JHJ, Ranjan D, Oakley JG, Anderson MH, Greenough JA, Bonazza R (2009) Computations in 3D for shock-induced distortion of a light spherical gas inhomogeneity. Shock Waves 28:1169–1174

Orth CD (2003) VISTA: a vehicle for interplanetary space transport application powered by inertial confinement fusion. University of California, Lawrence Livermore National Laboratory, Report UCRL-LR-110500, in final preparation

Prestridge K, Vorobieff P, Rightley PM, Benjamin RF (2000a) Validation of an instability growth model using particle image velocimetry measurements. Phys Rev Lett 84:4353–4356

Prestridge K, Rightley PM, Vorobieff P, Benjamin RF, Kurnit NA (2000b) Simultaneous density-field visualization and PIV of a shock-accelerated gas curtain. Exp Fluids 29:339–346

Ranjan D, Anderson M, Oakley J, Bonazza R (2005) Experimental investigation of a strongly shocked gas bubble. Phys Rev Lett 94:184507

Ranjan D, Niederhaus JHJ, Oakley JG, Anderson MH, Greenough JA, Bonazza R (2008) Experimental and numerical investigation of shock-induced distortion of a spherical gas inhomogeneity. Phys Scr 2008:014020

Ranjan D, Oakley J, Bonazza R (2011) Shock-bubble interactions. Annu Rev Fluid Mech 43:117–140

Richtmyer RD (1960) Taylor instability in shock acceleration of compressible fluids. Commun Pure Appl Math 13:297–319

Robey HF, Kane JO, Remington BA, Drake RP, Hurricane OA, Louis H, Wallace RJ, Knauer J, Keiter P, Arnett D, Ryutov DD (2001) An experimental testbed for the study of hydrodynamic issues in supernovae. Phys Plasmas 8:2446

Robey HF, Boehly TR, Celliers PM, Eggert JH, Hicks D et al (2012) Shock timing experiments on the National Ignition Facility: initial results and comparison with simulation. Phys Plasmas 19:042706

Samtaney R, Zabusky NJ (1994) Circulation deposition on shock-accelerated planar and curved density-stratified interfaces: models and scaling laws. J Fluid Mech 269:45–78

Smith AV, Holder DA, Barton CJ, Morris AP, Youngs DL (2001) Shock tube experiments on Richtmyer–Meshkov instability across a chevron profiled interface. In: 8th international workshop on the physics of compressible turbulent mixing, Pasedena, CA

Sturtevant B (1987) Rayleigh–Taylor instability in compressible fluids. In: 16th international symposium on shock tubes and waves. Aachen, West Germany, pp 89–100

Taylor G (1950) The instability of liquid surfaces when accelerated in a direction perpendicular to their planes. Proc R Soc Lond A 201:192–196

Vetter M, Sturtevant B (1995) Experiments on the Richtmyer–Meshkov instability of an air/SF 6 interface. Shock Waves 4:247–252

Vorobieff P, Anderson M, Conroy J, White R, Truman CR, Kumar S (2011) Vortex formation in a shock-accelerated gas induced by particle seeding. Phys Rev Lett 106:184503

Weber C, Haehn N, Oakley J, Rothamer D, Bonazza R (2012) Turbulent mixing measurements in the Richtmyer–Meshkov instability. Phys Fluids 24:074105

White R, Conroy J, Anderson M, Vorobieff P, Truman RC, Kumar S (2011) Oblique shock interaction with a gas cylinder. Bulletin of the American Physical Society. APS, Baltimore, MD

Zhang S, Peng G, Zabusky NJ (2005) Vortex dynamics and baroclinically forced inhomogeneous turbulence for shock—planar heavy curtain interactions. J Turbul 6:1–29